Microchannel deformations due to solvent-induced PDMS swelling†

Rémi Dangla,[a] François Gallaire[b] and Charles N. Baroud*[a]

Received 23rd February 2010, Accepted 24th June 2010
DOI: 10.1039/c003504a

The compatibility of polydimethylsiloxane (PDMS) channels with certain solvents is a well known problem of soft lithography techniques, in particular when it leads to the swelling of the PDMS blocks. However, little is known about the modification of microchannel geometries when they are subjected to swelling solvents. Here, we experimentally measure the deformations of the roof of PDMS microchannels due to such solvents. The dynamics of impregnation of the solvents in PDMS and its relation to volume dilation are first addressed in a model experiment, allowing the precise measurement of the diffusion coefficients of oils in PDMS. When Hexadecane, a swelling solvent, fills a microchannel 1 mm in width and 50 μm in height, we measure that the channel roof bends inwards and takes a parabolic shape with a maximum deformation of 7 μm. The amplitude of the subsidence is found to increase with the channel width, reaching 28 μm for a 2 mm wide test section. On the other hand, perfluorinated oils do not swell the PDMS and the microchannel geometry is not affected by the presence of perfluorodecalin. Finally, we observe that the trajectories of droplets flowing in this microchannel are strongly affected by the deformations: drops carried by swelling oils are pushed towards the edges of the channel while those carried by non-swelling oils remain in the channel center.

I. Introduction

In recent years, polydimethylsiloxane (PDMS) has emerged as the material of choice for rapid, low cost fabrication of microfluidic channels. This is due to the many advantages of PDMS, particularly its transparency and biocompatibility, in addition to the development of standard protocols for its fabrication.[1,2] This has allowed an explosion of interest in microfluidics by reducing the costs and complexity of fabricating microchannels.

However, PDMS presents a few characteristics which can limit its usefulness. It is a rubber elastic material[3] with a low Young's modulus $E \sim 1$ MPa and a high Poisson ratio $\nu = 0.5$, making microchannels highly flexible and compliant. As a result, structures of extreme aspect ratios are difficult to fabricate: tall pillars bend and buckle while wide microchannels sag and collapse.[4] Additionally, recent studies have shown that even stable geometries may significantly deform when the imposed flow pressures reach 10^5 Pa.[5–7]

A second drawback arises from the porous nature of PDMS, which leads to compatibility issues with some solvents.[8] Indeed, the absorption of certain liquids in the polymer matrix can lead to departures from the dry geometry of a microchannel. The rubber-like PDMS expands when a swelling solvent diffuses into the material, in an analogous fashion to heat diffusion and thermal expansion in elastic solids. The extent of the swelling of an isolated sheet is characterized by the swelling coefficient at saturation S_∞ which measures the ratio of its swollen length over its dry length. Typical values of S_∞ are in the range of 1.05 to 1.20, meaning that solvents can induce strains of up to 20%.[8]

Deformations of this magnitude have also been reported for PDMS microchannels, by observing the changes in the size and shape of the channels on microscopy images.[9,10] However, quantitative measurements of the microchannel deformation in the third dimension have proved difficult to obtain, although such information is of major importance for any microfluidic application that relies on a precise knowledge of the flow profile, for example when the shear stress on the wall must be known.[11]

In this paper, we study the deformation of PDMS microchannels when placed in contact with swelling oils. The swelling characteristics of the oils (S_∞ and the diffusion coefficient D) are first determined by analyzing the size of isolated PDMS sheets in a bath of oil. The height profile of microchannels is then obtained, when those are placed in contact with a swelling oil, and compared with the case of non-swelling solvents. The measurements are achieved by adapting an optical method, initially developed for fluid free surfaces,[12] which compares the displacement of a pattern between two images (*before* and *after*). Finally, we demonstrate that the swelling is responsible for deviations of droplet trajectories as they flow in a deformed microchannel.

Below, we begin by describing the experimental setup and protocol in Section II. This is followed, in Section III, by an explanation of the synthetic Schlieren method which is used to obtain the channel deformations. The results are presented in three parts: First the swelling characteristics of the oils are presented, followed by the shape of microchannels when in contact with these oils. Finally, we demonstrate the effect of the deformation on the motion of droplets in swollen channels.

II. Experimental setup and protocol

The microfluidic devices are fabricated in PDMS (Dow Corning SYLGARD 184, 1/10 ratio of curing agent to bulk material)

---

[a] *LadHyX and department of Mechanics, Ecole Polytechnique, CNRS, 91128 Palaiseau Cedex, France. E-mail: baroud@ladhyx.polytechnique.fr*
[b] *Laboratory of Fluid Mechanics and Instabilities (LFMI), Ecole Polytechnique Fédérale de Lausanne (EPFL), CH-1015 Lausanne, Switzerland*

† Electronic supplementary information (ESI) available: Derivations of eqn (4) and eqn (5), supplementary data and supplementary movie. See DOI: 10.1039/c003504a

using standard soft lithography techniques.[13,14] They are sealed onto a glass slide of thickness $h_g = 1.1$ mm by plasma bonding. The microchannels have a nominal height of $h_c = 50$ µm and the PDMS blocks have a global thickness h_P between 4 and 5 mm, as sketched in Fig. 1. Two solvents, hexadecane or perfluorodecalin (PFD), are used as the swelling and non-swelling oils in the microchannel experiments. They are injected into the channel by capillary suction, by depositing a drop at one of the channel entrances. The test sections whose deformations are measured have a length $L = 6$ mm and widths w of either 1 mm, 1.5 mm or 2 mm. They are connected to the entrance and exit through the main channel which is 100 µm in width.

The height profile of a test section is measured using a synthetic Schlieren approach, in which the surfaces of the PDMS act as lenses that refract a fixed pattern. By analyzing the image of this pattern seen through the PDMS, before and after the swelling, the local curvature of the surfaces can be reconstructed. This method has previously been used to observe deformations of a single free liquid surface[12] but works with any deformed refracting interface. Schematically, the refracted image is compared to a reference image using a Digital Image Correlation (DIC) algorithm to determine the apparent displacement field $\delta\vec{r}$ of the pattern, which is related to the gradient of the height profile of the deformed surface. The deformations are then reconstructed by numerically integrating the slope thus measured in two dimensions.

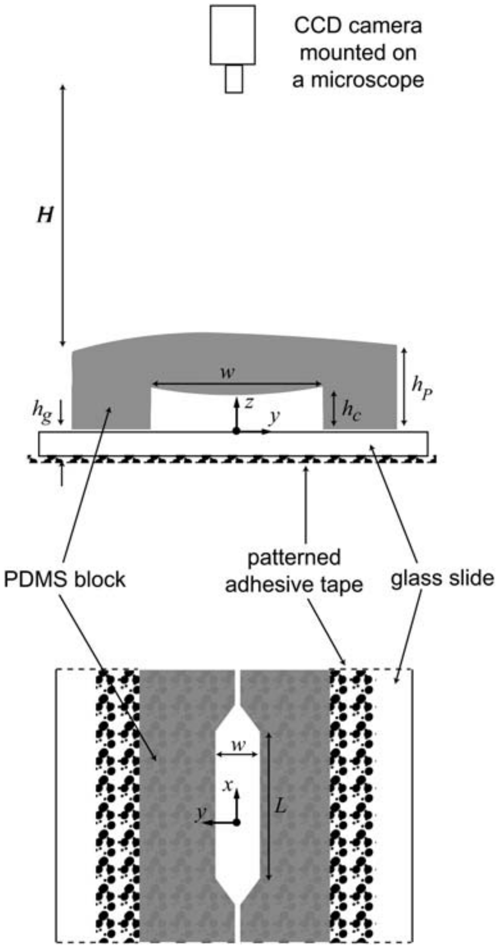

Fig. 1 Cross-section (top) and top view (bottom) of a microchannel test section, displaying the synthetic Schlieren experimental setup. The cross-section is not to scale.

The imaged pattern is obtained by fixing adhesive tape (3M Scotch Magic Tape) under the glass slide, as sketched in Fig. 1, and using its inherent texture. These patterns are visualized through a channel's test section using a digital camera mounted on a low magnification (3× to 5×) stereo microscope with backlighting. A typical image is shown in Fig. 2.a, where the microchannel walls are visible, in addition to the grainy texture to be tracked. The field of observation is a square, 3 mm to 5 mm in width depending on magnification, and the microscope's objective is at a distance $H \approx 7$ cm from the PDMS block. The DIC analysis to obtain the apparent displacement field is performed using the commercial software *DaVis* (LaVision). Multipass iterations with a decreasing window size and a 50% overlap are used for the computations of the correlation functions, leading to a displacement field defined on a 128×128 grid, with a spatial resolution ranging between 24.2 µm and 40.8 µm.

The experimental protocol consists of first preparing a microchannel and placing it on the apparatus described above. The field of observation is chosen such that the test section and the inlet channel are visible, then a reference image of the pattern is taken, as shown on Fig. 2.a. The solvent is then allowed into the microchannel and the device is monitored for 5 h by taking an image every 3 min. During this time, the solvent diffuses into the solid and evaporates into the atmosphere, leading to continuous variations of the observed pattern. These variations can be followed in Fig. 2.b which shows a space–time diagram extracted from a typical experiment. On this image, the horizontal axis represents time and the vertical axis gives the gray values measured along the line $A - A'$ in each image. Pattern displacements, which are a result of swelling induced surface deformations, can be qualitatively visualized in this way (see also movie in the ESI†).

III. Surface reconstruction

A typical experiment can be divided into two distinct periods, as pointed out on the spatio-temporal graph. During period 1, from $t = 0$ to $t = 90$ min in the example of Fig. 2.b, the channel is filled with solvent and the pattern displacements are due to the deformation of the top PDMS–air interface only. Indeed, the optical indices of glass ($n_g = 1.47$), PDMS ($n_{PDMS} = 1.42$) and of the solvents ($n_{hexa} = 1.43$, $n_{PFD} = 1.30$) are all close together. Therefore, the bottom two interfaces (glass–solvent and solvent–PDMS) disappear and the channel walls become invisible as long as the channel is filled.

The situation in period 1 is therefore strictly identical to the one described by Moisy *et al.*[12] Because the camera is far above the microchannel ($w/H \ll 1$), rays passing by the field of observation and reaching the objective are all nearly parallel. As they pass through the deformed interface, they are refracted at an angle proportional to the local slope of the interface. Hence, a point I of the pattern is actually seen by the camera as the point I', at a distance $\delta\vec{r}_1$ from its original position, as sketched in Fig. 3.a. The slope of the top surface is given by the gradient of the height deformations $\vec{\nabla} h'_P$ and, for small deformations ($h'_P/h_P \ll 1$), it is related to the apparent displacement field $\delta\vec{r}_1$ by

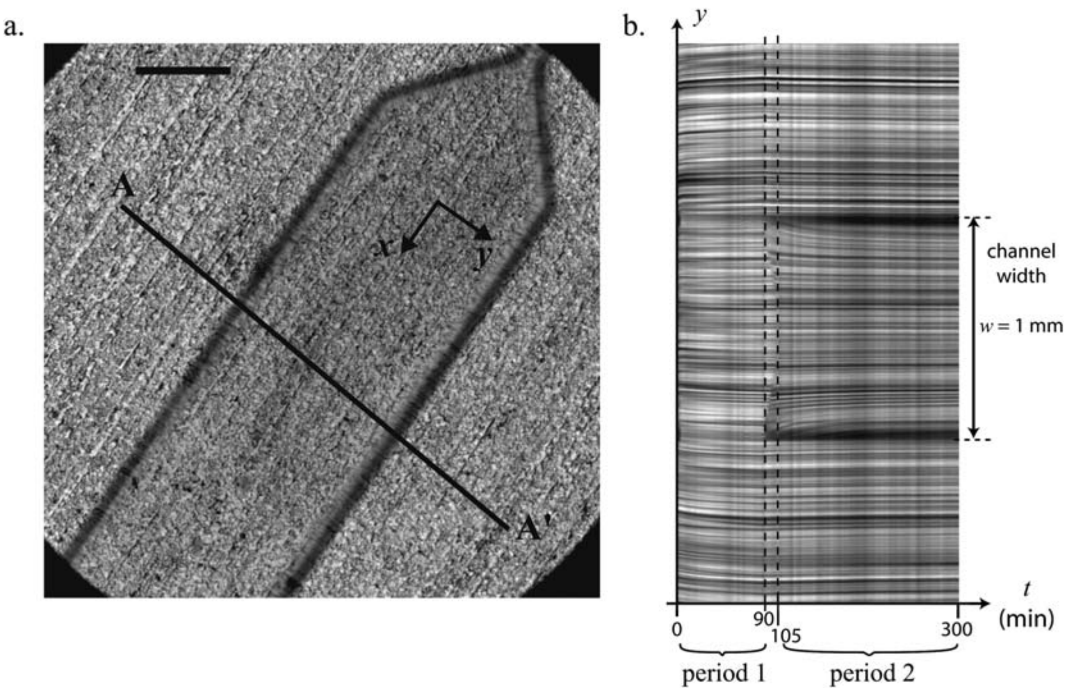

Fig. 2 a. Reference image of a channel taken before a swelling experiment, featuring the main test section of width $w = 1$ mm and the narrow inlet channel. The scale bar represents 500 μm. b. Space–time diagram showing the evolution of the pixel gray values along the axis ($A - A'$) of the reference image. The channel is filled with hexadecane from $t = 0$ min to $t = 90$ min and it is empty after $t = 105$ min.

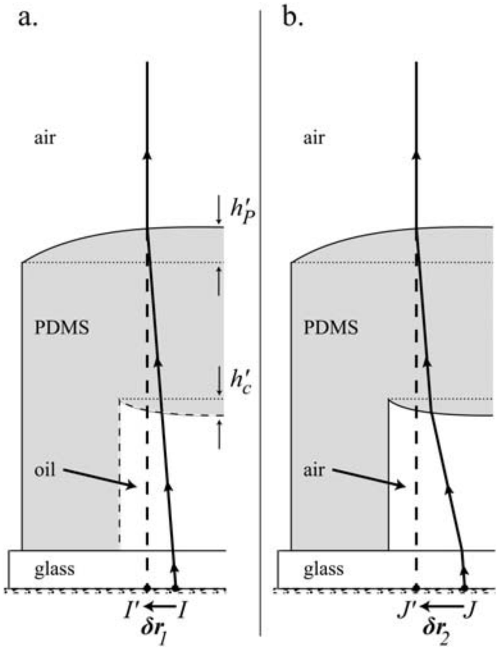

Fig. 3 Refraction of light rays by a deformed microchannel. The initial geometry is sketched by the dotted lines. a: The channel is filled with a solvent of matching optical index. The two bottom interfaces (dashed interfaces) disappear. The ray passing by I is refracted by the top surface and is seen as passing by I', inducing the apparent displacement $\delta\vec{r}_1$. b: The channel is filled with air. The ray is refracted by three interfaces, including two potentially deformed surfaces. Point J has an image at J', inducing the apparent displacement $\delta\vec{r}_2$.

$$\vec{\nabla} h'_P = \left(\frac{1}{H} - \frac{1}{h_1^*}\right)\delta\vec{r}_1 , \qquad (1)$$

where $h_1^* = (1 - n_{air}/n_{PDMS})(h_P + n_{PDMS}/n_{oil} \cdot h_c + n_{PDMS}/n_g \cdot h_g)$.

When using a stereomicroscope, this relation is modified by the fact that the optical axis of the microscope $\vec{n}$ is not aligned with the vertical axis $\vec{z}$ of the channel. The resulting viewing angle θ, typically around 10°, is characterized by its projections θ_x and θ_y on the in-plane axis $(\vec{x},\vec{y})$. A consequence of this non-alignment is a blur in the image near the vertical wall. To limit this drawback, the channel is aligned with the viewing angle, *i.e.* setting $\theta_y = 0$. A second consequence is a correction to the relationship between the apparent displacement field $\delta\vec{r}_1$ and the refracting interface slope $\vec{\nabla} h'_P$, yielding

$$\vec{\nabla} h'_P = \left(\frac{1}{H} - \frac{1}{h_1^*}\right) \cdot \left(\delta\vec{r_1} - \delta_\theta \vec{x}\right) , \qquad (2)$$

where $\delta_\theta = h_c\,[\tan(\sin^{-1}(1/n_{oil} \sin\theta)) - \tan\theta]$. This small correction does not modify the qualitative features but improves the homogeneity of the measured deformation.

Period 1 is followed by a short transition period, from $t = 90$ min to $t = 105$ min, during which the microchannel is partially empty. This translates to a sudden reappearance of the channel walls and to complex movements of the patterns on Fig. 2.b. However, the channel remains in contact with the swelling solvent during the transition (see movie in the ESI†).

The second period begins when the microchannel is completely emptied due to absorption and evaporation, at $t = 105$ min in Fig. 2.b. During period 2, the PDMS block is no longer in contact with the swelling agent and the geometry relaxes back to its initial shape, as observed on the space–time diagram. Again, the first image in period 2 is compared with the initial reference image by DIC analysis and yields a second displacement field $\delta\vec{r}_2$.

During this period, the pattern is refracted by two deformed surfaces: the air–PDMS interface which forms the channel roof and the PDMS–air interface on top of the block, in addition to the flat glass–air surface, as sketched in Fig. 3.b. One must therefore write that the total displacement $\delta\vec{r}_2$ is the sum of three elementary displacements and it is related to the gradients of both surface deformations $\vec{\nabla} h'_P$ and $\vec{\nabla} h'_c$, which yields

$$\vec{\nabla} h_c^{'} = -\left(\frac{1}{h_2^*} - \frac{1}{H}\right)\delta\vec{r}_2 + \frac{1/h_2^* - 1/H}{1/h_3^* - 1/H}\vec{\nabla} h_P^{'}, \tag{3}$$

where $h_2{}^* = (1\text{–}n_{PDMS}/n_{air})(h_c + n_{air}/n_{glass} \cdot h_g)$ and $h_3{}^* = (1\text{–}n_{air}/n_{PDMS})(h_P + n_{PDMS}/n_{air} \cdot h_c + n_{PDMS}/n_g \cdot h_g)$. Here, effects of the viewing angle θ are already accounted for by the term $\rightarrow \nabla h'_P$ coming from eqn (2).

Calculating the shape of the channel roof therefore depends on the knowledge of the shape of the top PDMS surface, which we extract from the displacement field $\delta\vec{r}_1$, at the end of period 1. The numerical integration method provided by Moisy *et al.*[15] is performed twice, first using eqn (2) to reconstruct the profile of the top PDMS surface h'_P, then on eqn (3) to reveal the channel's height profile h'_c, thereby reconstructing the complete geometry of the swollen microchannel.

The overall measurement accuracy and absolute error are a combination of system and DIC uncertainties, the latter being well documented in the literature for Particle Image Velocimetry .[16] The interrogation windows were chosen so that the image of the patterned tape satisfies the criterion of 5 "dots" per interrogation window. The feature size is around 10 pixels, thus exceeding the optimal size of 2–3 pixels. Hence, DIC has an uncertainty of 5% approximately and induces an absolute error of 0.5 μm on the reconstructed height profile. Uncertainties in the experimental apparatus lie in the measurement of the effective heights (h_1^*, h_2^*, h_3^*) and in the estimation of the viewing angle θ_x. For the former, the glass slide and the microchannel have precise nominal heights and the PDMS block is measured for each channel with of precision of 0.1 mm. In addition, we measure a viewing angle $\theta_x = 9° \pm 1°$ for our setup. This leads to an overall accuracy estimated at 10%.

IV. Results

A. Characteristics of the diffusion and the dynamics of swelling

To characterize the amplitude of PDMS swelling by solvents, Lee *et al.*[8] measured the swelling coefficient S_∞ for a number of organic solvents: this coefficient is defined as the ratio of the length L_∞ of a PDMS piece saturated by the solvent over its initial length L_0 before swelling. We conduct similar measurements for hexadecane, silicone V100 oil and paraffin oil. A thin square of PDMS (1 cm × 1 cm × 1 mm) is placed inside a Petri dish filled with the solvent of choice and is photographed during more than 12 h using a digital camera and a macro objective. On each image (3008 × 2000 pixels, 1100 pixels/cm), the width $L(t)$ of the PDMS square is measured and compared to the reference value L_0 to yield the amplitude and dynamics of swelling.

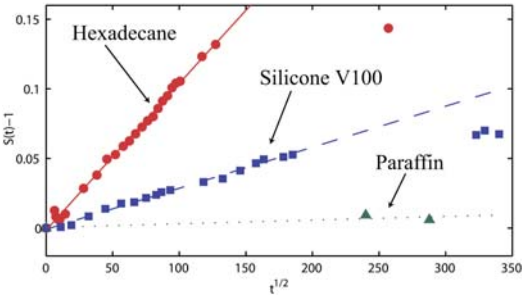

Fig. 4 Plots of the isotropic swelling coefficient $S(t)$ for hexadecane (●), silicone oil (■) and paraffin oil (▲) as a function of $\sqrt{t}$. The lines correspond to a linear fit before saturation.

The dynamics of swelling is linked to the absorption of the solvent into PDMS, which is a diffusive process, characterized by a diffusion coefficient D.[17] Modeling solvent diffusion and the deformations induced by local swelling in a thin PDMS sheet shows that the length of the sheet $L(t)$ evolves as

$$\frac{L(t)}{L_0} - 1 = (S_\infty - 1)\frac{2}{d}\sqrt{\frac{Dt}{\pi}}, \tag{4}$$

where d is the thickness of the PDMS sheet (see ESI for the derivation of this equation†). Eqn (4), which is valid before saturation occurs, can be used to estimate the diffusion coefficient D.

Accordingly, the transient swelling ratio $S(t) = L(t)/L_0$ is plotted as a function of $\sqrt{t}$ for hexadecane, silicone and paraffin oils in Fig. 4. The swelling coefficient at saturation S_∞ is evaluated from the steady state values of $S(t)$. Swelling is observed for hexadecane and silicone oil only. Next, the values of $\left[S(\sqrt{t}) - 1\right]$ are fitted with a linear law for early times. Fig. 4 shows a good agreement between the data points and the linear fit for both swelling oils, which validates the theoretical model used to compute eqn (4). Hence, the slope β of the fit can be used to evaluate the diffusion coefficient D of the solvent:

$$D = \pi\left(\frac{\beta d}{2(S_\infty - 1)}\right)^2. \tag{5}$$

The extracted values for S_∞ and D are listed in Table 1. They show good agreement with previous measurements for other carbon or silicone chains.[8,18–20]

The diffusion coefficient D is useful to estimate the time τ necessary for the microchannel to reach its swollen steady state. It is reasonable to assume that the system locally reaches its equilibrium shape when the PDMS has swollen over a layer of

Table 1 Swelling coefficients S_∞ and diffusion constant D

	S_∞	$D/\text{m}^2\ \text{s}^{-1}$
PFD	1.00 [a]	none
Paraffin oil	1.00 ± 0.01	none
Silicone V100	1.08 ± 0.01	$10 \pm 1 \times 10^{-12}$
Hexadecane	1.14 ± 0.01	$44 \pm 4 \times 10^{-12}$
n-Heptane	1.34 [a]	$13\text{–}70 \times 10^{-12}$ [b]

[a] Extracted from ref. 8. [b] Extracted from ref. 20.

thickness comparable to that of the microchannel height h_c. This will occur over a time determined by the diffusion of oil into PDMS, $\tau \propto h_c^2/D$. For a 50 μm-deep microchannel swollen with hexadecane or silicone oil, τ is on the order of 5 min, which is very short compared to the duration of period 1. We may therefore assume that our measurements of the microchannel deformations correspond to the swollen steady state.

B. Microchannel deformations

We follow the experimental protocol of Section 2 and perform an experiment using hexadecane on a test section of width $w = 1$ mm. Eqn (2) is first integrated taking $\theta_x = 9°$ to obtain the relative deformation of the top PDMS surface, which is shown in Fig. 5.b. This surface bends outwards away from the glass wall, with an amplitude of 10 μm above the microchannel. While these deformations are negligible for a PDMS block of thickness $h_P \approx 4$ mm, they become significant when compared with the thickness of a second microchannel which may be stacked over the first one, for instance in multilayer microfluidic devices.[2]

Next, the height profile of the channel h_c' is computed using eqn (3) at the beginning of period 2. This is done by injecting the deformations h_P', obtained at the end of period 1. The assumption that the top surface of the block has not significantly changed during the transition between the two periods is justified by noting that the pattern movements are small during this time lapse, as seen on the space–time plot of Fig. 2.b. The resulting swollen height profile h_c' is shown in Fig. 5.a. The roof of the test section is found to deform into the microchannel, displaying a transverse subsidence whose amplitude varies between 6 μm and 7 μm along the x-axis.

On the other hand, the narrow 100 μm-wide injection channel is not significantly deformed by swelling ($h_c'/h_c < 1\%$), while the subsidence rapidly increases with the channel width in the

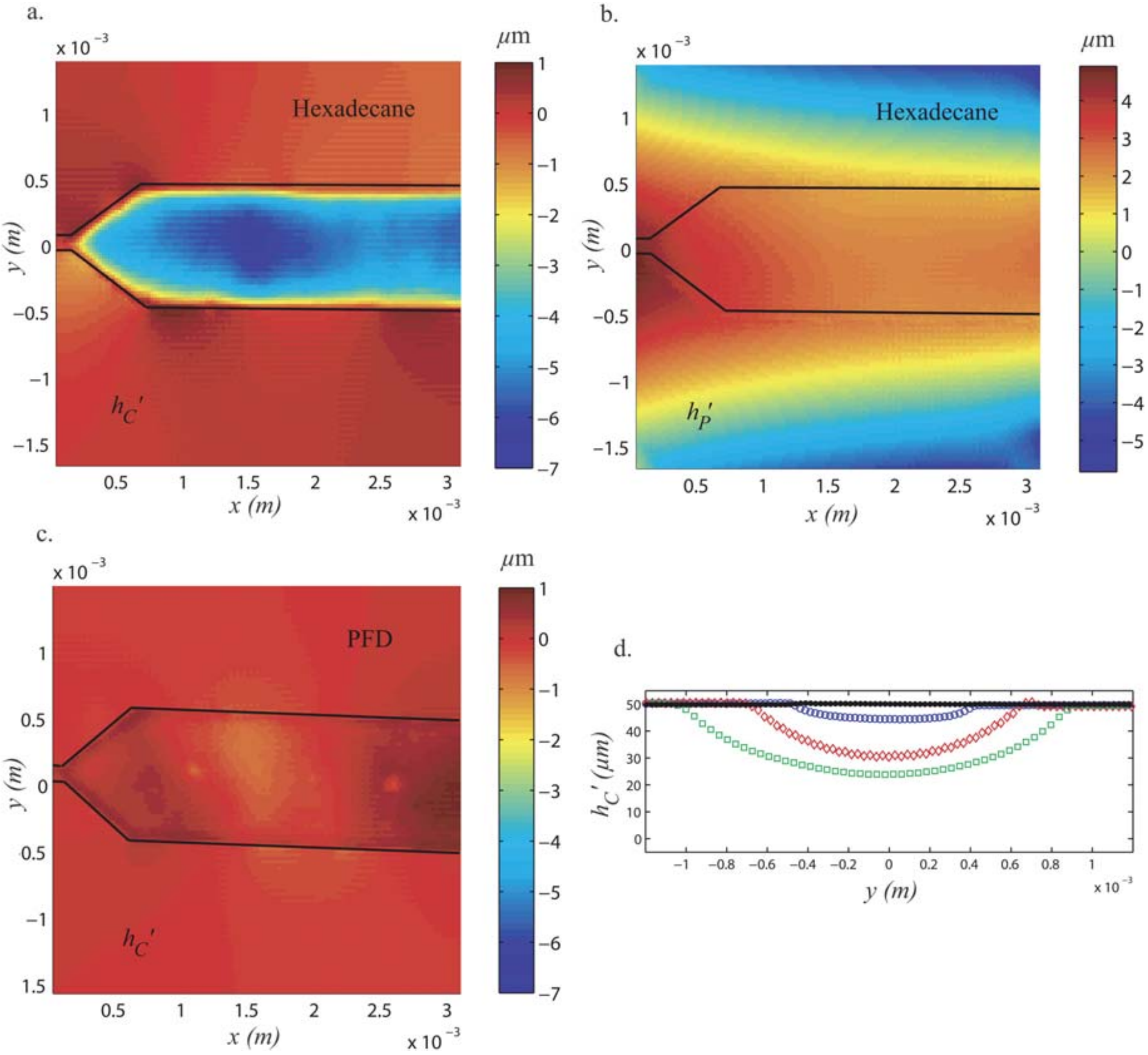

Fig. 5 Deformations of microchannels measured by the Synthetic Schlieren method. The position of the channel is outlined by solid lines. (a) Height profile h_c' of the roof of the test section swollen by hexadecane. (b) Height profile h_P' of the top surface of the PDMS block swollen by hexadecane. (c) Height profile h_c' the test section roof after PFD injection. (d) Transverse height profiles $h_c'(y)$ of the main test sections averaged along the x-axis for channels of widths 1 mm (○), 1.5 mm (◇) and 2 mm (□) swollen by hexadecane, and for a channel of width 1 mm after PFD injection (●).

diverging region, indicating that deformations are highly dependent on the channel's local aspect ratio $\alpha = w(x)/h_c$, in agreement with ref. 6.

To further investigate the influence of the channel's width, we perform experiments on test sections of width $w = 1.5$ mm and $w = 2$ mm. Again, we measure a subsidence of the channel roof, as seen on the height profiles (see ESI for figures†). The deformations for the three widths investigated are compared by averaging the subsidence along the length of the channel, in the x direction. The resulting profiles are plotted on Fig. 5.d and we observe that the amplitude of the deformations increases from 7 μm for $w = 1$ mm to 20 μm and 28 μm for $w = 1.5$ mm and $w = 2$ mm, respectively. In addition, an experiment on a 3 mm wide test section reveals that parts of the channel collapse, indicating that the deformations are larger than 50 μm for this width.

In contrast, the observed deformations are below the noise level of 0.5 μm when the experiments are performed using the non-swelling PFD, as shown on Fig.5.c. This is further confirmed since the height variations that are observed are mostly located near the channel edges where the vertical walls blur the images and introduce further errors into the DIC analysis. The averaged height profile for this case is also plotted in Fig. 5.d, showing no discernible height variation along the y-axis. This control experiment confirms that the deformations measured using hexadecane are indeed due to the swelling of the PDMS block.

C. Effect of deformations on droplet trajectories

The effect of depth variations on the flow in a microchannel has already been studied in the case of single phase flows. Indeed, slight deformations in the channel geometries have been shown to significantly influence the flow within it, for instance in the production of three-dimensional flow profiles,[21] in the amplification of the Taylor–Aris dispersion for pressure driven flows[22] or in the modification of the pressure *vs.* flow rate relationship.[7] Here, we observe the effect of the subsidence on the transport of droplets as they travel in the 1 mm wide test section. To this end, drops of water in oil are produced in a flow-focusing geometry[9] which is operated in a regime to produce large drops. In this way, the drops are flattened when they flow through the test section and are thus sensitive to the height variations.

We chose silicone oil (swelling solvent) and paraffin oil (non-swelling) as the carrier fluids for the study of droplet dynamics because these oils enable controlled droplet formation and injection under identical hydrodynamic and capillary conditions. Indeed, the two liquids have similar viscosities ($\nu_{sil} = 100$ cP and $\nu_{par} = 130$ cP) and interfacial tensions ($\gamma_{sil} = 0.25$ N m^{-1} and $\gamma_{par} = 0.25$ N m^{-1}). Drops are made and transported by the two fluids while keeping the flow rates and droplet radii similar, as shown on Fig. 6.

If the test section's geometry is unperturbed, droplets are expected to follow straight trajectories along the channel's centerline as they would in a perfect Hele-Shaw cell.[23,24] This behavior is indeed observed in Fig. 6.a which displays the trajectory of a water droplet in paraffin oil by superposing successive images of the droplet train. These drops follow the centerline of the channel and exit without feeling the presence of the side walls.

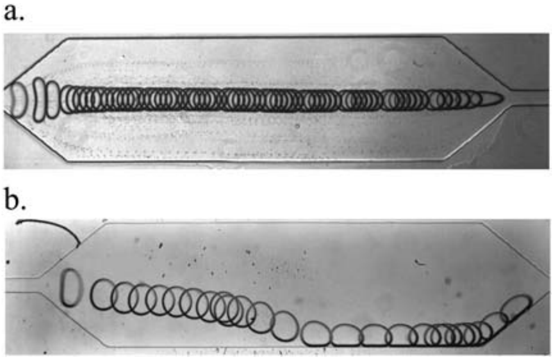

Fig. 6 Water droplets are advected from left to right along the large microchannel by a second carrier fluid. By superposing a few successive images taken using a high speed camera, the trajectories of the droplets are qualitatively visualized: (a) straight trajectory for paraffin oil ($Q = 1.1$ μL min^{-1} and $R = 100$ μm). (b) bent trajectory with transverse migration toward the side wall for silicone V100 oil ($Q = 3.0$ μL min^{-1} and $R = 130$ μm).

In contrast, drops carried by Silicone oil follow different trajectories, as shown in Fig. 6.b. These drops begin to deviate from the channel centerline as they enter the diverging section and they flow out of the test section along the side wall. Drops flowing at different flow rates make contact with the side walls at different locations, with faster drops advancing further before touching the sides. However, all drops deviate from the centerline before exiting the channel.

The physical reason for the trajectory modification can be understood in simple intuitive terms by considering the surface energy of the drop: Although the volume of each drop is fixed after its formation, its surface area varies as its shape changes. Recall that the smallest surface area for a drop of a given volume is given by a spherical shape, such that a flattened drop has an increased surface area and consequently an increased surface energy. By moving towards the side of the channel, where the subsidence is minimum, the drop minimizes its surface area by approaching a spherical shape. The migration of the drops towards the side walls therefore corresponds to a migration to the area of minimum confinement and minimum surface energy.

V. Summary and discussion

The synthetic Schlieren method developed to measure the deformations of PDMS microchannels only requires a low magnification microscope and adhesive tape. It is a simple and cost effective alternative to confocal or fluorescence microscopy with comparable resolution and precision. It is however limited to volatile liquids for two reasons. First, period 1 is excessively long for non-volatile liquids and the channel is not revealed in reasonable time. Second, the deformations of the microchannel are obtained at the beginning of period 2 when the liquid fully leaves the channel, and not when the channel is filled with the solvent at the end of period 1. The assumption that the roof of the channel has not deformed during this time is only valid if the transition period is short, which is the case for volatile liquids only.

The auxiliary experiment used to measure the swelling characteristics of a solvent into PDMS is easy to implement. Through an analysis of the time evolution of the PDMS sheet, this experiment gives access to the swelling coefficient S_∞ and also to the diffusion coefficient D of the oil, which is a key parameter in estimating the time necessary for establishment of a swollen steady state.

Finally, the swelling of PDMS by a solvent induces a subsidence of the microchannel. The amplitude of the deformations increases with the width of the channels, exceeding 50% of the channel's thickness for the widest channel measured here. This subsidence modifies the trajectories of pancake droplets and pushes them towards the sides of the wide test section, where the channel has a maximum depth. This behavior can be intuitively explained by energy arguments and a precise prediction of the trajectory based on such arguments is the subject of our current research.

Acknowledgements

The authors are grateful to Basile Audoly for help in deriving the model which leads to eqn (4) and Hervé Turlier for developing the microchannel geometry.

References

1 D. Duffy, J. McDonald, O. Schueller and G. Whitesides, *Anal. Chem.*, 1998, **70**, 4974–4984.
2 M. A. Unger, H. P. Chou, T. Thorsen, A. Scherer and S. R. Quake, *Science*, 2000, **288**, 113–116.
3 J. C. Lotters, W. Olthuis, P. H. Veltink and P. Bergveld, *J. Micromech. Microeng.*, 1997, **7**, 145–147.
4 C. Y. Hui, A. Jagota, Y. Y. Lin and E. J. Kramer, *Langmuir*, 2002, **18**, 1394–1407.
5 M. A. Holden, S. Kumar, A. Beskok and P. S. Cremer, *J. Micromech. Microeng.*, 2003, **13**, 412–418.
6 T. Gervais, J. El-Ali, A. Gunther and K. F. Jensen, *Lab Chip*, 2006, **6**, 500–507.
7 B. S. Hardy, K. Uechi, J. Zhen and H. P. Kavehpour, *Lab Chip*, 2009, **9**, 935–938.
8 J. Lee, C. Park and G. M. Whitesides, *Anal. Chem.*, 2003, **75**, 6544–6554.
9 S. L. Anna, N. Bontoux and H. A. Stone, *Appl. Phys. Lett.*, 2003, **82**, 364–366.
10 S. Vanapalli, A. Banpurkar, D. Ende, M. Duits and F. Mugele, *Lab Chip*, 2009, **9**, 982–990.
11 E. Young and C. Simmons, *Lab Chip*, 2010, **10**, 143–160.
12 F. Moisy, M. Rabaud and K. Salsac, *Exp. Fluids*, 2009, **46**, 1021–1036.
13 J. C. McDonald, D. C. Duffy, J. R. Anderson, C. D. T., H. Wu, O. J. A. Schueller and G. M. Whitesides, *Electrophoresis*, 2000, **21**, 27–40.
14 K. Stephan, P. Pittet, L. Renaud, P. Kleimann, P. Morin, N. Ouaini and R. Ferrigno, *J. Micromech. Microeng.*, 2007, **17**, N69–N74.
15 F. Moisy and M. Rabaud, *Free-Surface Synthetic Schlieren (FS-SS): a tutorial*, 2008.
16 M. Raffel, C. E. Willert, S. T. Wereley and J. Kompenhans, *Particle Image Velocimetry*, Springer, 1998.
17 E. Sultan and A. Boudaoud, *J. Appl. Mech.*, 2008, **75**, 051002.
18 E. Favre, P. Schaetzel, Q. Nguygen, R. Clement and J. Neel, *J. Membr. Sci.*, 1994, **92**, 169–184.
19 M. Chandak, Y. Lin, W. Ji and R. Higgins, *J. Appl. Polym. Sci.*, 1998, **67**, 165–175.
20 C. Zhao, J. Li, Z. Jiang and C. Chen, *Eur. Polym. J.*, 2006, **42**, 615–624.
21 E. Lauga, A. Stroock and H. Stone, *Phys. Fluids*, 2004, **16**, 3051–3062.
22 D. Dutta, A. Ramachandran and D. T. Leighton, *Microfluid. Nanofluid.*, 2006, **2**, 275–290.
23 G. I. Taylor and T. G. Saffman, *Q. J. Mech. Appl. Math.*, 1959, **12**, 265–279.
24 A. R. Kopf-Sill and G. Homsy, *Phys. Fluids*, 1988, **31**, 18–26.